

## Photonic Gap Antennas Based on High-Index-Contrast Slot Waveguides

Ashutosh Patri<sup>1</sup>, Kévin G. Cognée,<sup>2</sup> Louis Haeberlé<sup>3</sup>, Vinod Menon,<sup>2</sup> Christophe Caloz<sup>1</sup>,<sup>4</sup> and Stéphane Kéna-Cohen<sup>1,3,\*</sup>

<sup>1</sup>*Department of Electrical Engineering, Polytechnique Montréal, Montréal, Québec H3T 1J4, Canada*

<sup>2</sup>*Center for Discovery and Innovation, City College of New York, New York, New York 10031, USA*

<sup>3</sup>*Department of Engineering Physics, Polytechnique Montréal, Montréal, Québec H3T 1J4, Canada*

<sup>4</sup>*Department of Electrical Engineering, KU Leuven, B-3001 Leuven, Belgium*

(Received 7 April 2021; revised 26 July 2021; accepted 31 August 2021; published 29 October 2021)

Optical antennas made of low-loss dielectrics have several advantages over plasmonic antennas, including high radiative quantum efficiency, negligible heating, and excellent photostability. However, due to weak spatial confinement, conventional dielectric antennas fail to offer light-matter interaction strengths on par with those of plasmonic antennas. We propose here an all-dielectric antenna configuration that can support strongly confined modes ( $V \sim 10^{-4} \lambda_0^3$ ) while maintaining unity antenna quantum efficiency. This configuration consists of a high-index pillar structure with a transverse gap that is filled with a low-index material, where the contrast of indices induces a strong enhancement of the electric field perpendicular to the gap. We provide a detailed explanation of the operational principle of such photonic gap antennas (PGAs) based on the dispersion relation of symmetric and asymmetric horizontal slot waveguides. To discuss the properties of PGAs, we consider silicon pillars with air or the polymer CYTOP as the gap material. We show by full-wave simulations that PGAs with an emitter embedded in the gap can enhance the spontaneous emission rate by a factor of approximately 1000 for air gaps and approximately 400 for CYTOP gaps over a spectral bandwidth of  $\Delta\lambda \approx 300$  nm at  $\lambda = 1.25 \mu\text{m}$ . Furthermore, the PGAs can be designed to provide unidirectional out-of-plane radiation across a substantial portion of their spectral bandwidth. This is achieved by setting the position of the gap at an optimized off-centered position of the pillar so as to properly break the vertical symmetry of the structure. We also demonstrate that, when acting as receivers, PGAs can lead to a near-field intensity enhancement by a factor of approximately 3000 for air gaps and approximately 1200 for CYTOP gaps.

DOI: 10.1103/PhysRevApplied.16.044065

### I. INTRODUCTION

The development of optical antennas has progressed tremendously over the past two decades. Similar to their long-wavelength (radio and microwave) counterparts, optical antennas convert far-field electromagnetic radiation into localized near-field components and vice versa. While transmission in long-wavelength antennas is driven by alternating electrical currents, optical antennas are typically excited by nanoscale emitters such as atoms, molecules, or quantum dots. Therefore, an efficient extraction of electromagnetic radiation requires a strong localization of the near-field energy. To achieve this, the vast majority of theoretical and experimental work has focused on the use of subwavelength metallic antennas [1]. Metals at visible and infrared frequencies support surface plasmons that allow for deep-subwavelength (approximately  $\lambda/10$ ) localization of oscillating electric

fields. This is obtained by converting the electric field energy—the source of capacitance—into kinetic energy of free electrons—the source of kinetic inductance [2]. This contrasts with the case of long-wavelength and dielectric antennas, where energy oscillates mostly between the electric and magnetic fields. The ability of plasmonic antennas to manipulate or enhance the emission of nearby emitters has been found useful both for light-emitting devices [3] and state-of-the-art single-photon sources [4]. Moreover, their ability to concentrate light has found important applications; for instance, in sensing, nonlinear optics, integrated photonics, and imaging [5–9].

An important drawback of plasmonic antennas is the presence of Ohmic losses due to various scattering processes that occur within the electron gas. This can lead to considerable heat generation, resulting in melting or irreversible structural alteration of the antenna and thermochemical destruction of the nearby matter [10–13]. Moreover, losses within the metal implicitly limit the quantum efficiency of emitters, a phenomenon that

\*s.kena-cohen@polymtl.ca

severely hampers their utilization in applications where efficiency (loss) is important [14]. This decreases the radiation efficiency or antenna quantum efficiency,  $\eta = P_{\text{sca}}/(P_{\text{sca}} + P_{\text{abs}})$ , where  $P_{\text{sca}}$  and  $P_{\text{abs}}$  are the power scattered (accepted) and absorbed by the antenna, respectively [15]. Although inefficient emitters can see their internal quantum efficiency increase via coupling to plasmonic antennas—because the antenna quantum efficiency can exceed that of the emitter—emitters that are *a priori* efficient inevitably see their quantum efficiency lowered.

A strategy to avoid the Ohmic losses in plasmonic antennas has been to use, instead, nanoantennas made of high-refractive-index dielectrics, where  $P_{\text{abs}} \approx 0$  allows for radiation efficiencies equal to unity. Silicon nanospheres, for example, support strong Mie resonances in the visible and near infrared [16–18]. However, since light in a dielectric material is bound by the diffraction limit, the volumetric modes (or bulk modes) of such antennas tend to suffer from very weak spatial confinement as compared to the surface modes of their metallic counterparts [19]. In addition, bulk modes do not readily allow for the placement of emitters or analytes at the position of maximum near-field intensity [20]. Recently, the use of multielement all-dielectric structures such as dimers [21,22] or oligomers [23], where the dipole modes of individual elements hybridize, has been demonstrated to provide strong field confinement in the interelement spacing region. Single-element gapped structures that can support nonradiating anapole modes [24,25] with high quality factors have also been proposed to overcome these drawbacks. Nevertheless, the achievable electric field confinement in such designs has remained limited by the lateral size of the nanoscale voids incorporated in the structure, the resolution of which is dictated by the available nanolithography technology. Finally, for many applications, out-of-plane unidirectional radiation is desirable. Symmetric structures [24,25] inherently possess nondirectional radiation patterns. Although breaking this symmetry to achieve directionality is possible with multiple lithography steps, this places stringent fabrication constraints [26].

In this work, we propose dielectric antennas, which we refer to as photonic gap antennas (PGAs) based on Fabry-Perot-type resonances of slot-waveguide modes [27]. We exploit the high-field-confinement capability of such dielectric gap modes [28–35] using a simple multi-layer pillar architecture, as shown in Fig. 1(a), and demonstrate spontaneous-emission-rate (SER) enhancements  $> 1000$  for an emitter embedded within the gap. We design silicon- ( $n = 3.53$ ) nanopillar-based PGAs consisting of a gap layer of air ( $n = 1$ ) or CYTOP ( $n = 1.33$ ). The adoption of horizontal gap layers in PGAs, realizable by simple deposition processes, avoids the fabrication constraints of lithography-based techniques [36–38]. We study the propagating eigenmodes of both vertically symmetric and asymmetric horizontal slot waveguides and show that the

corresponding resonant modes of finite-length structures can interfere with each other to realize unidirectional out-of-plane radiation. This directionality spans over a substantial portion of the emission-enhancement bandwidth of  $\Delta\lambda \approx 300$  nm. We also discuss the scattering properties of PGAs, in the receiving regime, for an incident plane wave and demonstrate that a field-intensity enhancement as high as approximately 3000 can be achieved.

## II. PGA DESIGN PRINCIPLE

To illustrate the physical mechanism underpinning PGAs and to remind the reader of the slot-waveguide concept, we begin by examining the dispersion relation of rectangular silicon waveguides, shown in Fig. 1(b). The dispersion equation for the eigenmodes of the slot-waveguide structures can be found in Refs. [27] and [39]. The colored lines in Figs. 1(c) and 1(d) correspond to configurations without a gap, with a centered (along  $z$ ) air gap and with an off-centered air gap, each 2 nm thick. The ratios ( $t_1/t_2$ ) of the below-gap thickness ( $t_1$ ) to the above-gap thickness ( $t_2$ ) of silicon are 1 and 3, respectively, for the symmetric and the asymmetric slot waveguides. The width of the waveguides is set to 240 nm and the total height including the gap thickness is set to 582 nm. Propagation in the waveguide is along the  $x$  direction, with a propagation constant of  $k_x$ , i.e., along the direction normal to the cross sections shown in the inset of Fig. 1(d). We consider transverse magnetic polarization, so that the electric field orientation ( $E_z$ ) is perpendicular to the plane of the gap layer. Since the normal component of the electric displacement field,  $\mathbf{D} = \epsilon\mathbf{E}$ , is continuous at the two dielectric interfaces, the  $E_z$  component of the quasi-TM modes is stronger in the low-index region of the gap than in the high-index region of the waveguide. The field strength within the air-gap layer is proportional to  $E_{z,\text{air}} = (\epsilon_{\text{Si}}/\epsilon_{\text{air}})E_{z,\text{Si}}$  and can be further maximized by increasing the difference between the permittivity of the gap material and the waveguide material. In the spectral range of interest, we have two eigenmodes for the slot waveguides, the  $\text{TM}_0$  and  $\text{TM}_1$  modes, originating from the even ( $\text{TM}_0$ ) and odd ( $\text{TM}_1$ ) modes of the unperturbed silicon waveguide. We note that the presence of the gap only weakly perturbs the dispersion relation of the silicon waveguide. In Figs. 2(a), 2(c), and 2(e), we plot the electric field mode profiles in each of these waveguides at frequencies corresponding to the normalized propagation constant of  $k_x\ell/2\pi = 0.5$ , where  $\ell = 250$  nm is chosen to give a resonance in the  $\lambda = 1.0 - 1.5 \mu\text{m}$  range.

To realize PGAs, as in Fig. 1(a), the slot waveguides must be truncated so as to satisfy the Fabry-Perot resonance condition  $k_x\ell/2\pi = m/2$  for a positive integer value of  $m$  and a finite length,  $\ell$ , along the propagation direction [40]. This condition is highlighted by a vertical dashed line in Figs. 1(c) and 1(d), which corresponds to the  $m = 1$ ,

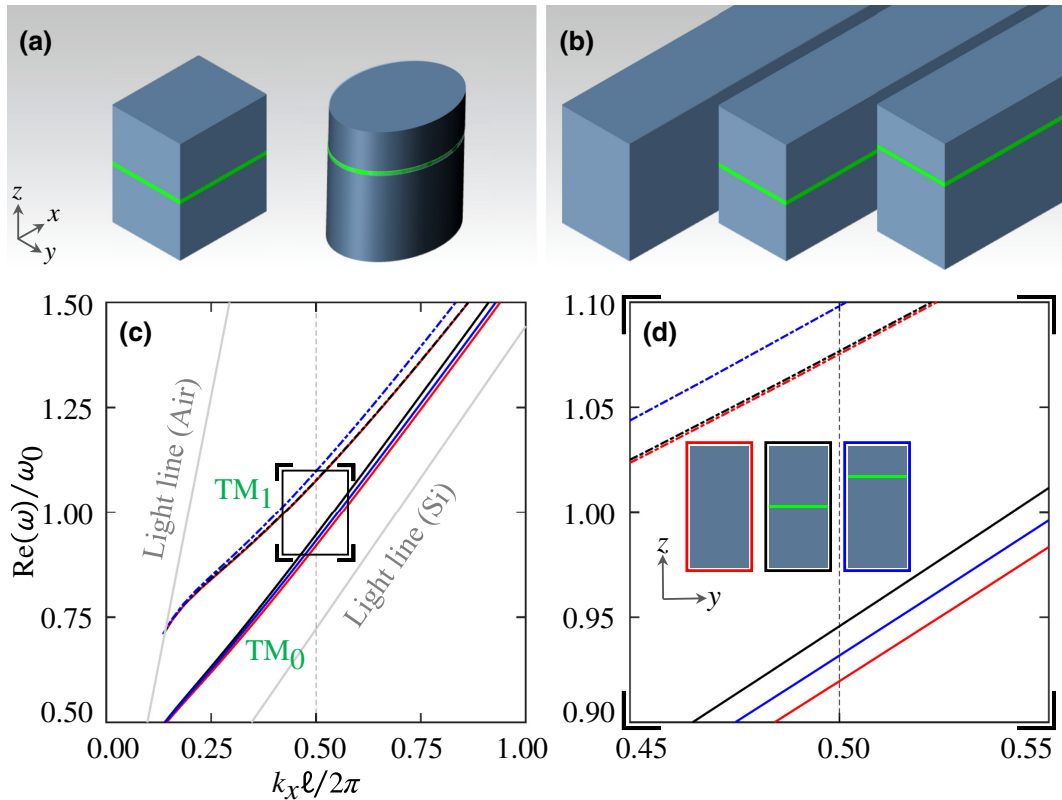


FIG. 1. Photonic gap antennas (PGAs) and the dispersion relation of their infinite-length waveguide counterparts. (a) A perspective view of different PGA structures: a symmetric rectangular PGA (left) and an asymmetric elliptical PGA (right). (b) A perspective view of an infinite-length (along  $x$ ) conventional silicon waveguide (left), a symmetric slot waveguide (center), and an asymmetric slot waveguide (right). (c) The dispersion relation for the two lowest quasi-TM eigenmodes (electric field along the  $z$  axis), showing the normalized real angular frequency,  $\text{Re}(\omega)/\omega_0$ , where  $\omega_0 = 2\pi(235)$  THz, as a function of the normalized propagation constant,  $k_x \ell / 2\pi$ , where  $\ell = 250$  nm. These relations are plotted for the conventional silicon waveguide (red), the symmetric slot waveguide (black), and the asymmetric slot waveguide (blue). The corresponding cross sections are shown as insets in (d). The waveguides are composed of silicon, with an air gap, with a gap thickness of 2 nm. The height (including the gap) and width of the waveguide cross sections are 582 nm (along  $z$ ) and 240 nm (along  $y$ ), respectively. The solid gray lines show the light lines for bulk air and silicon. The vertical dashed line at  $k_x \ell / 2\pi = 0.5$  intersects the dispersion curves of the waveguides at their respective resonant frequencies for a finite-length ( $\ell = 250$  nm) of the structure along the  $x$  axis. (d) An enlarged portion of the dispersion relation in (c), identified by a rectangle, highlighting changes due to the incorporation of the gap layer.

$\ell = 250$  nm resonance condition. In Fig. 2(a), we show the mode profiles for the even ( $\text{TM}_0$ ) and odd ( $\text{TM}_1$ ) eigenmodes of the conventional silicon waveguide with no gap. For the symmetric slot waveguide, shown in Fig. 2(c), the  $E_z$  component of the  $\text{TM}_0$  mode becomes strongly concentrated in the gap. From the dispersion relation in Fig. 1, we also see that the effective index ( $n_{\text{eff}}$ ) for this mode differs slightly from that of the conventional silicon waveguide. In contrast, in the case of the  $\text{TM}_1$  mode, the field profile and  $n_{\text{eff}}$  values are indistinguishable compared to those of the conventional silicon waveguide. This is a consequence of the vanishing  $E_{z,\text{Si}}$  component at the gap position. For the asymmetric slot waveguide, both TM modes have different mode profiles and  $n_{\text{eff}}$  values than the corresponding modes in the conventional silicon waveguide. From Fig. 2(e), we note that  $E_{z,\text{Si}}$  for the  $\text{TM}_1$  mode of the asymmetric slot

waveguide has a nonzero value at the gap position and that both the  $\text{TM}_0$  and  $\text{TM}_1$  modes have their maximum field values located near the gap. Hence, in contrast to the symmetric case, an emitter embedded inside the gap of a resonating asymmetric slot waveguide will strongly interact with both modes.

To evaluate the electric-field-confinement capability of the gap modes in the PGAs and to compare them with conventional Si antenna, we calculate the quality factors (temporal confinement) and the mode volumes (spatial confinement) of the structures. The quality factors ( $Q$  factors) for both resonant modes of the PGAs and the conventional dielectric antenna are relatively low ( $Q_{\text{TM}_0} \approx 7$ ,  $Q_{\text{TM}_1} \approx 14$ ), which is to be expected due to their strong radiative leakage. This indicates that the field-confinement capability of these antennas is a direct consequence of

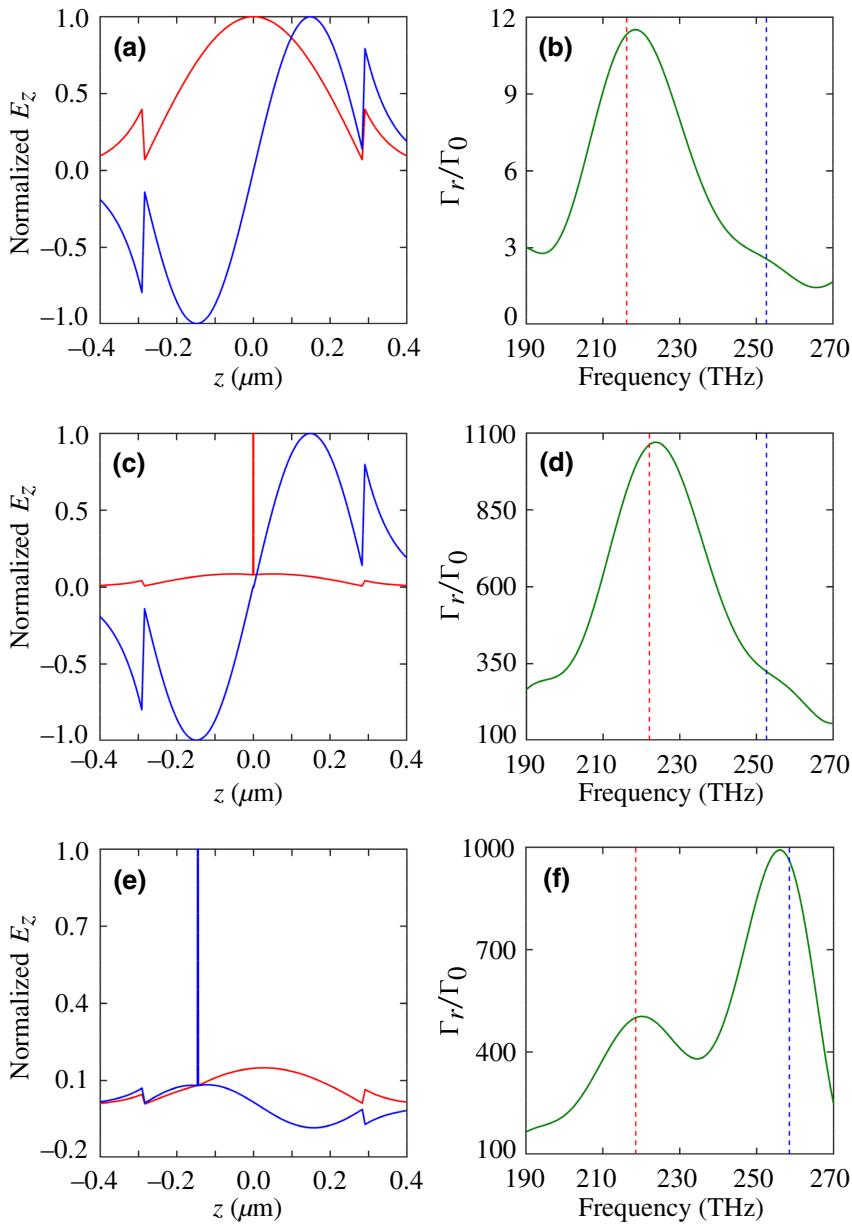


FIG. 2. The normalized  $E_z$  of the eigen-mode profiles for the infinite-length waveguides in Fig. 1(b) and SER enhancement factors for the corresponding PGAs (finite-length waveguide sections). The  $E_z$  components for the TM<sub>0</sub> (red) and TM<sub>1</sub> (blue) modes are shown at their respective resonant frequencies for (a) the conventional silicon waveguide, (c) the symmetric slot waveguide, and (e) the asymmetric slot waveguide. (b),(d),(f) The SER enhancement factors versus the frequency for the corresponding finite-length ( $\ell = 250 \text{ nm}$ ) waveguide structures of (a), (c), and (e), respectively. The vertical dashed lines in (b), (d), and (f) are at the resonant frequencies of the TM<sub>0</sub> (red) and the TM<sub>1</sub> (blue) mode calculated from the dispersion relation illustrated in Figs. 1(c) and 1(d).

smaller mode volumes (tighter spatial confinement). We calculate the mode volume at the position of maximum field intensity of each localized mode, which occurs in the middle of the gap layer and 110 nm away from the  $y$ - $z$  plane of symmetry along the  $x$  axis. We use the quasinormal-mode (QNM) formalism [41,42] to calculate the mode volumes unambiguously, while also addressing the normalization issues [43] arising from the mode-volume definition in leaky cavities. QNM theory yields complex mode volumes,  $\tilde{V}_m$ , that are characteristic of non-Hermitian resonators [44]. Given that when  $|\text{Re}(\tilde{V}_m)|^2 >> |\text{Im}(\tilde{V}_m)|^2$ , which is the case here, the real part contributes to the maximum field confinement on resonance [42], we only report the real parts, which have a simpler physical interpretation. The resonant TM<sub>0</sub> mode in

the symmetric PGA has a mode volume of  $\tilde{V}_{\text{PGA}} \approx 5 \times 10^{-4} \lambda_0^3$ , whereas the resonant TM<sub>0</sub> and TM<sub>1</sub> modes of the asymmetric PGA have mode volumes of approximately  $13 \times 10^{-4} \lambda_0^3$  and approximately  $9 \times 10^{-4} \lambda_0^3$ , respectively, where  $\lambda_0$  denotes the free-space wavelengths at corresponding resonant frequencies of the modes. In contrast, the TM<sub>0</sub> of the conventional dielectric antenna shows  $\tilde{V}_{\text{Si}} \approx 4 \times 10^{-3} \lambda_0^3$ . By comparing the mode volumes, we find the conventional antenna to be approximately 100 times  $[(\epsilon_{\text{Si}}/\epsilon_{\text{air}})(\tilde{V}_{\text{Si}}/\tilde{V}_{\text{PGA}})]$  weaker in spatial confinement of light than the PGA. Note that the tight field confinement provided by PGAs is even on par with that provided by plasmonic antennas [8,45] but without Ohmic losses.

### III. RESULTS AND DISCUSSION

#### A. Enhancement of spontaneous emission

Resonant photonic structures can enhance the radiative decay rate of an emitter by virtue of the spectral and spatial confinement of electromagnetic radiation. In the quantum picture, this change in SER comes about from a modification of the amplitude of vacuum-field fluctuations at the position and orientation of the emitter, within its bandwidth. This is usually quantified by the change in the projected local density of optical states [46]. Classically, this effect can be understood as being due to the action of the scattered field due to the resonator, which acts back on the dipole (emitter) and can be quantified by measuring the change in input impedance of the dipole [46]. The SER enhancement factor is described by  $\Gamma_r/\Gamma_0$ , where  $\Gamma_r$  is the radiative decay rate of the emitter in the presence of the resonating structure and  $\Gamma_0$  is the decay rate of the same emitter in free space.

To study the SER enhancement of an emitter within the rectangular-cross-section PGAs described in the previous section and to compare their enhancement capability with the conventional dielectric antenna without gap, we place a 2-nm-long and infinitesimally thin current dipole at the position where the  $E_z$  component is maximal for the resonating  $TM_0$  mode of each structure. The dipole moment is oriented along the  $z$  axis to maximize the interaction with the resonating modes. Finite-difference time-domain (FDTD) three-dimensional (3D) simulations are used to calculate the total radiated power from the real part of the impedance,  $\Re(Z)$ , of the dipole [15], i.e.,  $P = \frac{1}{2}|I|^2\Re(Z)$ , where  $|I|$  is the amplitude of the applied current in the dipole. In the absence of material loss, the nonradiative part of the decay rate is zero and the SER enhancement factor becomes  $\Gamma_r/\Gamma_0 = P/P_0$ , where  $P$  and  $P_0$  are the powers radiated by the dipole in the vicinity of the PGA and in free space, respectively. In Figs. 2(b), 2(d), and 2(f), we plot the SER enhancement factors for the conventional dielectric antenna, the symmetric PGA, and the asymmetric PGA, respectively. We find that the PGAs show a SER that is 2 orders of magnitude ( $\times 10^2$ ) faster than for an emitter in the conventional Si dielectric antenna. This is a direct consequence of their reduced mode volumes. Compared to an emitter in free space, this corresponds to a SER enhancement by 3 orders of magnitude ( $\times 10^3$ ). Furthermore, the frequencies corresponding to the peaks in SER enhancement agree well with the resonant frequencies calculated from the waveguide dispersion relation in Fig. 1. These are shown as vertical dashed lines in Figs. 2(b), 2(d), and 2(f).

#### B. Introduction of elliptical PGAs

Although the rectangular pillars already highlight the fundamental features of PGAs, their performance can be

further improved by modifying the cross-section shape. For example, by tapering the rectangular waveguide along the  $y$  axis, the  $n_{\text{eff}}$  for both modes can be further reduced to approximately 1. This shifts the electromagnetic energy density from the high-index regions to the low-index regions and subsequently leads to increased spatial confinement in the gap. With this in mind, we replace the rectangular cross sections with elliptical ones (with their major axis aligning in the propagation direction of the initial rectangular slot waveguides), as shown in Fig. 3(a). To keep the resonance frequencies of the elliptical PGA the same as that of the rectangular one, the length along its major axis ( $x$ ) is increased to 300 nm while maintaining the length along the minor axis the same as the width of the rectangular PGA.

Elliptical PGAs with the same height and gap position as the symmetric and asymmetric rectangular PGAs can increase the SER enhancement factor by more than 20% for both resonant modes, as shown in Fig. 3(b), while keeping the resonant frequencies the same. The resonant  $TM_0$  mode in symmetric elliptical PGA and the resonant  $TM_1$  mode in an asymmetric elliptical PGA can provide a SER enhancement factor of approximately 1300 and approximately 1200, respectively. In addition, the gap position in an asymmetric elliptical PGA allows the embedded dipole emitter to radiate efficiently over  $\Delta\lambda > 250$  nm, via coupling to both resonant modes, with a SER enhancement factor  $> 500$ . The SER enhancement factors for the variation in the lateral position of the emitter (along the  $x$  axis, centered in the gap) are shown in Fig. S1 of the Supplemental Material [47]. First, we observe that even at the center of the PGA ( $x = 0$   $\mu\text{m}$ ), where the  $E_z$  component of the resonating  $TM_0$  and  $TM_1$  modes vanishes, there is still a considerable SER enhancement ( $\Gamma_r/\Gamma_0 \approx 85$ ). This is due to the coupling of the emitter to the nonresonating part of the TM-gap modes in the background [48], and the SER enhancement factor is equivalent to the case of an emitter embedded in an infinitely long slot waveguide [30]. Second, the region of maximal enhancement in PGAs lies near the edges of the gap layer. As a result, air-gap PGAs could be realized with a glass support structure at the center without impacting the maximum SER achievable (see Fig. S2 in the Supplemental Material [47]). In the following sections, we restrict our attention to elliptical PGAs, due to their superior performance over rectangular PGAs.

#### C. Radiation-pattern engineering

The radiation pattern of PGAs primarily depends on the spatial and spectral overlap between the free-space radiation modes and the waveguide modes on each facet of the structure. The resonant  $TM_0$  and  $TM_1$  modes are zero-order modes along the  $y$  axis and the corresponding mode profiles have a single antinode in this direction. Therefore, we can restrict our attention to a two-dimensional slice in

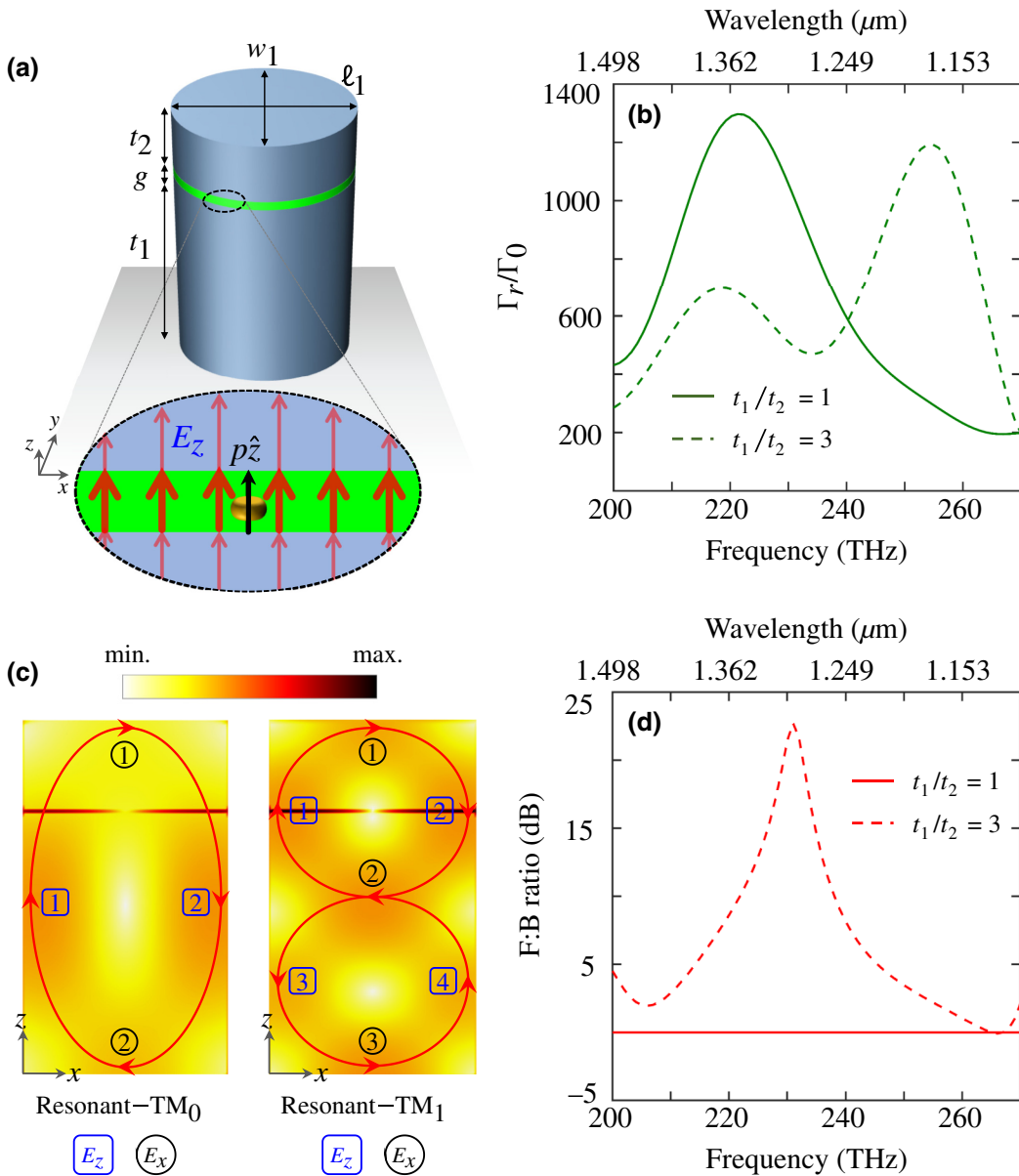


FIG. 3. The design and emission properties of elliptical PGAs. (a) A perspective view of the asymmetric elliptical PGA ( $t_1/t_2 = 3$ ) with design parameters (in nanometers)  $w_1 = 240$ ,  $\ell_1 = 300$ ,  $t_1 = 435$ ,  $t_2 = 145$ , and  $g = 2$  nm. The emitter is  $\hat{z}$  oriented and positioned within the gap layer 124 nm away from the vertical central axis of the structure along the  $x$  axis. (b) SER enhancement factors versus frequencies for the asymmetric PGA in (a) and the symmetric PGA with  $t_1/t_2 = 1$  ( $t_1 + t_2$  constant). (c) The electric field distribution in the central  $x$ - $z$  plane of the asymmetric PGA for the TM<sub>0</sub> (left) and TM<sub>1</sub> (right) modes. (d) The F:B ratio as a function of the frequency for asymmetric and symmetric PGAs.

the  $x$ - $z$  central plane of the antenna to understand the radiation pattern. In this plane, both the  $E_z$  and  $E_x$  components of the resonating TM<sub>0</sub> mode have a single antinode (even parity), as shown in Fig. 3(c) in the case of asymmetric PGAs ( $t_1/t_2 = 3$ ). Such a field distribution suggests that the resonating TM<sub>0</sub> mode can couple to plane waves propagating along the  $x$  and  $z$  axes ( $E_z$ , ① and ②—responsible for radiation in the  $-x$  direction and the  $+x$  direction, respectively;  $E_x$ , ① and ②—responsible for radiation in

the  $+z$  direction and the  $-z$  direction, respectively). In contrast, the  $E_x$  components of the resonating TM<sub>1</sub> mode have a single antinode and the  $E_z$  components have two antinodes of opposing sign (odd parity). Since these antinodes of the  $E_z$  components are within the silicon, they are spaced by a distance smaller than the half-wavelength in air and result in destructive interference along the  $x$  axis ( $E_z$ , ① and ③—responsible for null radiation in the  $-x$  direction;  $E_z$ , ② and ④—responsible for null radiation in

the  $+x$  direction). This maximizes the radiation of the resonant  $\text{TM}_1$  mode along the  $z$  axis due to coupling of the  $E_x$  components of the mode with propagating plane waves in that direction ( $E_x$ , ①—responsible for radiation in the  $+z$  direction;  $E_x$ , ③—responsible for radiation in the  $-z$  direction).

To maximize the collection efficiency of a nearby free-space optical system, PGAs should ideally radiate unidirectionally out of plane (here, in the  $-z$  direction). The symmetric PGAs behave as single-mode resonators supporting the  $\text{TM}_0$  mode, with negligible coupling of the emitter to the  $\text{TM}_1$  mode, and leak a significant amount of radiation along the  $\pm x$  directions in addition to the desired  $\pm z$  directions; therefore, they produce an omnidirectional radiation pattern. Offsetting the position of the gap allows for directionality. First, this allows coupling of the emitter to the  $\text{TM}_1$  mode, which ensures radiation predominantly along the  $\pm z$  directions while minimizing the radiation along the  $\pm x$  directions at the resonant frequency of the  $\text{TM}_1$  mode. Second, the asymmetric gap position leads to unequal perturbations of the  $E_x$  components of the modes along the  $z$  axis and realizes higher directionality in a preferred direction. For example, the asymmetric PGA, shown in Figs. 3(a) and 3(c), allows for strong excitation of the resonant  $\text{TM}_1$  mode. Additionally, the modal field distributions show a relatively strong  $E_x$  component near the bottom air-dielectric interface ( $E_x$ , ② and ③ in the case of resonant  $\text{TM}_0$  and  $\text{TM}_1$ , respectively.) compared to the one near the top air-dielectric interface ( $E_x$ , ① in the case of both resonant  $\text{TM}_0$  and  $\text{TM}_1$ ). To quantify the asymmetric radiation of PGAs along the  $z$  axis, we calculate the ratio of the power radiated along the  $-z$  direction (forward, F) to the power radiated along the  $+z$  direction (backward, B)—the F:B ratio. For the asymmetric PGA ( $t_1/t_2 = 3$ ), we observe a F:B ratio  $> 3$  dB, as shown in Fig. 3(d), for both the  $\text{TM}_0$  and the  $\text{TM}_1$  mode at their respective resonant frequencies [49].

Because of the low  $Q$  characterizing both resonant modes, emitters in the asymmetric PGAs can readily excite both simultaneously. For an emitter frequency in between the resonant frequencies of the two antenna modes, we observe a F:B ratio of 22 dB, as shown in Fig. 3(d), due to constructive interference along the  $-z$  direction and destructive interference along the  $+z$  direction. This phenomenon of directional radiation due to interference between modes has been studied extensively for Mie resonators such as silicon nanospheres, where the Kerker condition between electric and magnetic dipoles of the structure leads to unidirectional emission [50–52]. It turns out that the asymmetric PGA design with  $t_1/t_2 = 3$  offers a relatively low SER enhancement factor in the frequency range of the maximum F:B ratio. Fortunately, this can be improved by tuning the coupling strength of the emitter with the resonating  $\text{TM}_0$  and  $\text{TM}_1$  modes through the

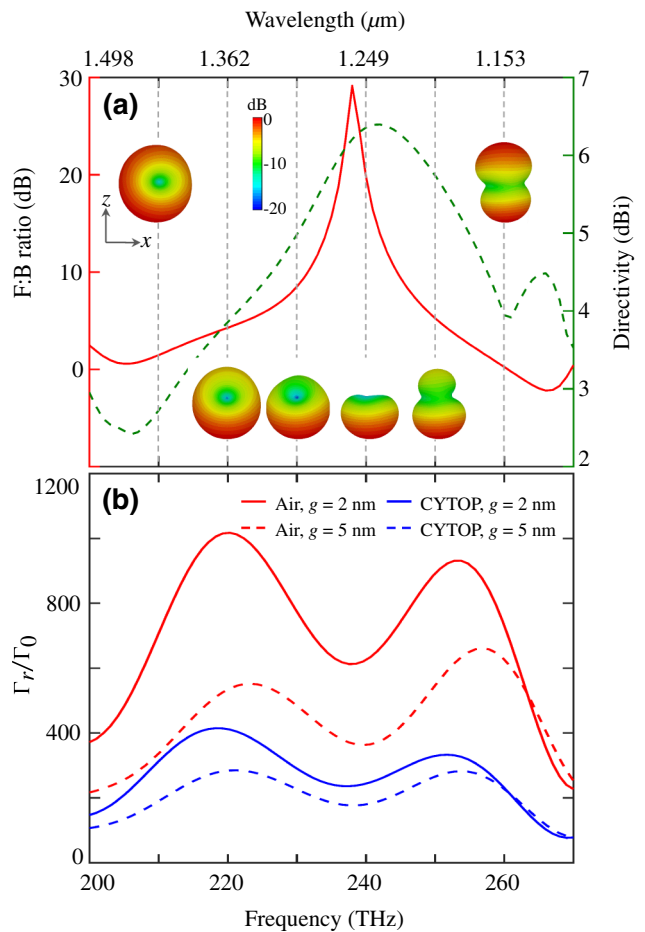


FIG. 4. The radiation properties of an asymmetric PGA with  $t_1/t_2 = 1.76$  and SER enhancement factors for different gap thicknesses and materials. The total thickness of silicon ( $t_1 + t_2$ ),  $w_1$  and  $\ell_1$  are the same as in Fig. 3(a). (a) The F:B ratio (left axis) and directivity (right axis) versus the frequency for the PGA with a 2-nm air gap. The insets show the radiation patterns of the PGA in the  $x$ - $z$  plane at the corresponding frequencies, with their maximum directivity normalized to 0 dB. (b) SER enhancement factors versus the frequency for the PGA with air gaps (red) and CYTOP gaps (blue) of thickness  $g = 2$  nm (solid lines) and  $g = 5$  nm (dashed lines).

choice of the gap position. For example, Fig. 4 shows results for an asymmetric PGA with  $t_1/t_2 = 1.76$  that can attain a SER enhancement factor of approximately 600 at an intermediate frequency, while radiating with a F:B ratio of 30 dB. This strategy also improves the spectral bandwidth of the PGA to  $\Delta\lambda = 315$  nm at  $\lambda = 1.25 \mu\text{m}$ . Note that the resonant frequencies of the structure remain unchanged when moving the gap to this new position due to the small changes in the corresponding  $n_{\text{eff}}$  of the slot-waveguide modes. This is in contrast to strategies where dielectric structures must be optimized to place the two resonant frequencies close to each other to achieve directionality [50,51].

The superposition of the  $\text{TM}_0$  and  $\text{TM}_1$  modes also allows for radiation leakage in the  $\pm z$  directions. For this purpose, it is essential to consider the antenna directivity in addition to its F:B ratio. In Fig. 4(a), we plot the directivity of the PGA (with  $t_1/t_2 = 1.76$ ) normalized to that of an isotropic antenna [53]. We obtain a maximum directivity of approximately 6.2 dBi near the frequency range of the maximum F:B ratio. The radiation pattern of this PGA in the  $x$ - $z$  plane (normalized to 0 dB) is shown at selected frequencies in the inset of Fig. 4(a). These results demonstrate that PGA can radiate directionally over a broad bandwidth toward the collection optics in the bottom ( $-z$  direction). To change the maximum radiation direction toward the top ( $+z$  direction), the antenna structure simply needs to be flipped upside down.

#### D. Influence of gap thickness and material

The performance of PGAs is primarily governed by the modal distribution near the gap region. This distribution can be tuned by varying the gap thickness, and the index contrast between the gap material and the pillar material. To study the impact of the parameters, we show additional results for PGA designs with a gap thickness of 5 nm or the use of CYTOP ( $n = 1.33$ ) as the gap material. For ultrathin films far from material resonances, previous work has suggested that nonlocal effects can be safely ignored [54,55]. To first order, the field in the subwavelength dielectric gap is homogeneous and when the gap size increases, the electromagnetic energy shifts to the higher index region, which increases the mode volumes. As shown in Fig. 4(b), thicker gaps and a lower index contrast both decrease the SER enhancement. We observe a SER enhancement that is approximately 2.5 times smaller ( $\Gamma_{\text{air}}/\Gamma_{\text{CYTOP}}$ ) for a 2 nm CYTOP gap as compared to that of an air gap. In contrast, the  $\Gamma_{\text{air}}/\Gamma_{\text{CYTOP}}$  becomes approximately 2 in the case of a 5-nm gap. This shows that the impact of the gap thickness on the SER is reduced for lower index contrasts. We also study the influence of a glass substrate ( $n = 1.50$ ) on the SER enhancement factors of PGAs with different gap thickness and materials and present the results in Fig. S3 in the Supplemental Material [47]. We note that due to substrate-induced asymmetry, both the SER enhancement factor and the F:B ratio can be improved further in the frequency range between the resonances.

#### E. PGAs as receivers

Light reception is the reciprocal of emission. As receivers, dielectric optical antennas collect radiation, which is then converted to oscillating electric and magnetic fields confined in the near field. The collection efficiency of an antenna can be characterized by its extinction cross section, whereas the conversion and concentration efficiencies can be characterized by the localized field (amplitude) enhancement or intensity enhancement factor. To study

these figures of merit for PGAs, we consider a linearly  $x$ -polarized plane wave incident on the PGAs. Since the PGAs are designed to efficiently radiate in the  $-z$  direction, the propagation of the incident plane wave is chosen in the reciprocal direction ( $+z$ ). Here, we report results for the symmetric and asymmetric PGAs ( $t_1/t_2 = 1, 1.76, 3$ ) with 2- and 5-nm-thick CYTOP gaps ( $g = 2, 5$ ). The corresponding results for the PGAs with air gaps are presented in Fig. S4 in the Supplemental Material [47].

The collection efficiency of an antenna relates the amount of power received,  $P_r$ , by the antenna to the incident plane-wave power density,  $S$ , i.e.,  $P_r/S$ . The received power can be expressed by  $P_r = SA_{\text{eff}}T$ , where  $A_{\text{eff}}$  is the effective aperture of the antenna in the direction of the incoming plane wave and  $T$  is the intensity transmission coefficient [56]. The parameter  $A_{\text{eff}} = \lambda^2 D/4\pi$  is a measure of normalized directivity, where  $D$  is the directivity of the antenna when receiving in the direction of plane-wave propagation. In the case of nanoscale antennas, measuring the received power is difficult from the antenna end; however, the scattered power,  $P_{\text{sca}}$ , can be measured instead. In the absence of Ohmic losses, the scattered power is the same as the received power ( $P_r = P_{\text{sca}} + P_{\text{abs}}$ ,  $P_{\text{abs}} = 0$ ). Therefore, the collection efficiency,  $P_r/S$ , of the antenna can be characterized by the extinction cross section (here, the same as the scattering cross section),  $\sigma_{\text{ext}} = \sigma_{\text{sca}} = P_{\text{sca}}/S$ . At the resonant frequencies of the structure,  $T \rightarrow 1$ , and  $\sigma_{\text{ext}}$  essentially depend on the  $A_{\text{eff}} \propto D$  of the antenna.

As shown in Fig. 5(a), we observe a relatively high  $\sigma_{\text{ext}}$  at the resonant frequency of the  $\text{TM}_1$  mode as compared to that of the  $\text{TM}_0$  mode. This is because the  $\text{TM}_1$  mode of the PGA has a higher directionality (bidirectional) in the  $-z$  direction compared to the  $\text{TM}_0$  mode (omnidirectional) [57]. At frequencies where the antenna is off resonance, the amount of received power ( $P_r$ ) decreases due to the lower transmission coefficient ( $T \ll 1$ ). Hence, in the frequency range between the two resonances of the structure,  $\sigma_{\text{ext}}$  decreases, in spite of the high directionality ( $D$ ). A parameter closely related to  $\sigma_{\text{sca}}$  ( $= \sigma_{\text{ext}}$ ) is the scattering efficiency  $Q_{\text{sca}} = \sigma_{\text{sca}}/C_g$ , which can be calculated for a geometric cross section  $C_g = 0.0565 \mu\text{m}^2$  of the PGA. We obtain a maximum  $Q_{\text{sca}}$  of approximately 30 for the case of symmetric PGA ( $t_1/t_2 = 1$ ) with a 5-nm CYTOP gap.

The near-field enhancement factor is defined as the ratio between the maximum electric field amplitude ( $|\mathbf{E}_{\text{max}}|$ ) in the vicinity of the PGA and the amplitude of the incident plane wave ( $|\mathbf{E}_{\text{inc}}|$ ). Higher values of the field enhancement factor are obtained when the PGA receives more power ( $\propto SA_{\text{eff}}T$ ) and stores it in a smaller 3D space for a longer time. In particular, symmetric PGAs ( $t_1/t_2 = 1$ ) receive a relatively high amount of power at the resonant frequency of the  $\text{TM}_1$  mode. However, this mode is a bulk mode (the same as that of the conventional dielectric pillar without a gap) and fails to store the energy within the gap. As shown in Fig. 5(b), this phenomenon leads to relatively

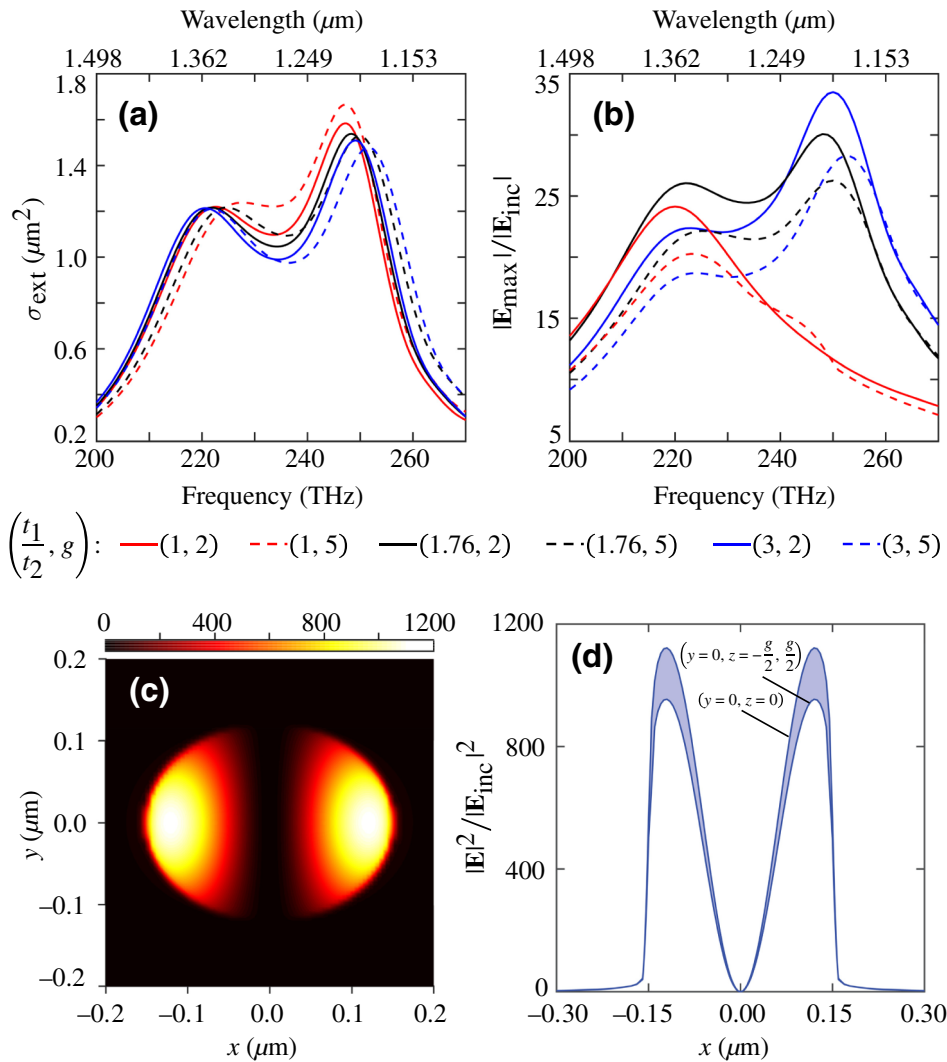


FIG. 5. The extinction cross sections and electric field enhancement factors of PGAs with a CYTOP gap. (a) The extinction cross section ( $\sigma_{\text{ext}} = \sigma_{\text{sca}}$ ) versus the frequency. (b) The field enhancement factor  $|E_{\text{max}}|/|E_{\text{inc}}|$  as a function of the frequency for elliptical PGAs, where the gap position and thickness are varied. The combined thickness of silicon ( $t_1 + t_2$ ),  $w_1$ , and  $\ell_1$  are the same as for the PGA in Fig. 3(a). (c) The near-field intensity distribution for the asymmetric PGA ( $t_1/t_2 = 3$ ) with  $g = 2$  nm on a plane parallel to  $x$ - $y$  plane and passing through the center of the gap layer. (d) The intensity distribution within the gap layer along the  $x$  axis at  $y = 0$ . The upper line of the shaded region represents the intensity profile at the center of the gap ( $z = 0$ ), whereas the lower bound represents the intensity profile near the CYTOP-Si boundaries ( $z = -g/2, g/2$ ). The field intensity increases from the bottom CYTOP-Si boundary to the center of the gap and decreases in a similar pattern up to the top CYTOP-Si boundary.

low field enhancements at the respective resonant frequencies. In contrast, the very same mode in asymmetric PGAs ( $t_1/t_2 = 3$ ) can strongly confine the near-field energy in the gap region and can have field enhancement factors as high as approximately 35 (intensity enhancement factor approximately 1200) for a 2-nm CYTOP gap and approximately 55 (intensity enhancement factor approximately 3000) for an air gap of the same thickness (for PGAs with air gaps, see Fig. S4 in the Supplemental Material [47]). As expected, this value decreases with an increasing value of the gap thickness. Similar to the transmission configuration, the receiving configuration of asymmetric PGAs allows for high field enhancement over a broad spectral bandwidth of  $\Delta\lambda \approx 300$  nm. For the asymmetric PGA ( $t_1/t_2 = 3, g = 2$  nm), we show in Fig. 5(c) the near-field intensity distribution in a plane parallel to the  $x$ - $y$  plane and passing through the center of the gap. We observe an essentially uniform distribution of intensity along the gap thickness from the intensity-distribution plot shown in Fig. 5(d).

#### IV. CONCLUSION

We present an all-dielectric optical antenna that can serve as a platform for engineering light-matter interaction on par with that of plasmonic antennas. PGAs exploit the properties of deep-subwavelength slot-waveguide modes both for strong spatial confinement and for unidirectional radiation over a broad spectrum. We show that the radiated power of a quantum emitter in free space can be improved by  $> 1000$  times by embedding it within the gap of PGA, while maintaining a quantum efficiency of approximately 100%. The use of all-dielectric structures rather than metallic ones becomes of increasing importance for applications that are sensitive to heating or require high quantum efficiency. In the receiving regime, PGAs can tightly confine the field of an incident plane wave with an intensity enhancement of up to approximately 3000. This can be useful both for interacting with localized emitters and for enhancing nonlinear effects in cases where heating from plasmonic antennas can be problematic. These

results are particularly compelling given the relative simplicity of the antenna structure. Our study could be further extended to improve these enhancement factors as well as the radiation directionality of PGAs by fabricating the antennas on a dielectric mirror or numerically optimizing the PGA cross section. In a separate paper, we consider the use of gaps with a vanishingly small refractive index ( $n \approx 0$ ) to explore the limit of spatial confinement using the gap modes. In that case, the nanopillar modes strongly hybridize with the epsilon-near-zero (ENZ) mode of the gap, leading to extremely efficient light-matter interaction and intrinsic unidirectional radiation [58].

## ACKNOWLEDGMENTS

This work was supported by the Natural Sciences and Engineering Council of Canada Strategic Grant program and the Canada Research Chairs program. The work at City College of New York was supported by National Science Foundation (NSF) QII-TAQS Grant No. 1936351.

- [1] L. Novotny and N. Van Hulst, Antennas for light, *Nat. Photonics* **5**, 83 (2011).
- [2] J. B. Khurgin and A. Boltasseva, Reflecting upon the losses in plasmonics and metamaterials, *MRS Bull.* **37**, 768 (2012).
- [3] K. L. Tsakmakidis, R. W. Boyd, E. Yablonovitch, and X. Zhang, Large spontaneous-emission enhancements in metallic nanostructures: Towards leds faster than lasers, *Opt. Express* **24**, 17916 (2016).
- [4] A. F. Koenderink, Single-photon nanoantennas, *ACS Photonics* **4**, 710 (2017).
- [5] R. D. Grober, R. J. Schoelkopf, and D. E. Prober, Optical antenna: Towards a unity efficiency near-field optical probe, *Appl. Phys. Lett.* **70**, 1354 (1997).
- [6] P. Bharadwaj, B. Deutsch, and L. Novotny, Optical antennas, *Adv. Opt. Photonics* **1**, 438 (2009).
- [7] M. Kauranen and A. V. Zayats, Nonlinear plasmonics, *Nat. Photonics* **6**, 737 (2012).
- [8] P. Biagioni, J.-S. Huang, and B. Hecht, Nanoantennas for visible and infrared radiation, *Rep. Prog. Phys.* **75**, 024402 (2012).
- [9] M. Agio and A. Alù, *Optical Antennas* (Cambridge University Press, Cambridge, 2013).
- [10] A. Kuhlicke, S. Schietinger, C. Matyssek, K. Busch, and O. Benson, *In situ* observation of plasmon tuning in a single gold nanoparticle during controlled melting, *Nano Lett.* **13**, 2041 (2013).
- [11] M. Caldarola, P. Albella, E. Cortés, M. Rahmani, T. Roschuk, G. Grinblat, R. F. Oulton, A. V. Bragas, and S. A. Maier, Non-plasmonic nanoantennas for surface enhanced spectroscopies with ultra-low heat conversion, *Nat. Commun.* **6**, 1 (2015).
- [12] M. Mahmoudi, S. E. Lohse, C. J. Murphy, A. Fathizadeh, A. Montazeri, and K. S. Suslick, Variation of protein corona composition of gold nanoparticles following plasmonic heating, *Nano Lett.* **14**, 6 (2014).
- [13] I. Alessandri and J. R. Lombardi, Enhanced Raman scattering with dielectrics, *Chem. Rev.* **116**, 14921 (2016).
- [14] W. Barnes, G. Björk, J. Gérard, P. Jonsson, J. Wasey, P. Worthing, and V. Zwiller, Solid-state single photon sources: Light collection strategies, *Eur. Phys. J. D* **18**, 197 (2002).
- [15] A. E. Krasnok, A. P. Slobozhanyuk, C. R. Simovski, S. A. Tretyakov, A. N. Poddubny, A. E. Miroshnichenko, Y. S. Kivshar, and P. A. Belov, An antenna model for the Purcell effect, *Sci. Rep.* **5**, 12956 (2015).
- [16] A. I. Kuznetsov, A. E. Miroshnichenko, M. L. Brongersma, Y. S. Kivshar, and B. Luk'yanchuk, Optically resonant dielectric nanostructures, *Science* **354**, aag2472 (2016).
- [17] D. Bouchet, M. Mivelle, J. Proust, B. Gallas, I. Ozerov, M. F. Garcia-Parajo, A. Gulinatti, I. Rech, Y. De Wilde, and N. Bonod *et al.*, Enhancement and Inhibition of Spontaneous Photon Emission by Resonant Silicon Nanoantennas, *Phys. Rev. Appl.* **6**, 064016 (2016).
- [18] A. Barreda, J. Saiz, F. González, F. Moreno, and P. Albella, Recent advances in high refractive index dielectric nanoantennas: Basics and applications, *AIP Adv.* **9**, 040701 (2019).
- [19] S. I. Bozhevolnyi and J. B. Khurgin, Fundamental limitations in spontaneous emission rate of single-photon sources, *Optica* **3**, 1418 (2016).
- [20] V. Rutckaia, F. Heyroth, A. Novikov, M. Shaleev, M. Petrov, and J. Schilling, Quantum dot emission driven by Mie resonances in silicon nanostructures, *Nano Lett.* **17**, 6886 (2017).
- [21] P. Albella, M. A. Poyli, M. K. Schmidt, S. A. Maier, F. Moreno, J. J. Sáenz, and J. Aizpurua, Low-loss electric and magnetic field-enhanced spectroscopy with subwavelength silicon dimers, *J. Phys. Chem. C* **117**, 13573 (2013).
- [22] R. Regmi, J. Berthelot, P. M. Winkler, M. Mivelle, J. Proust, F. Bedu, I. Ozerov, T. Begou, J. Lumeau, and H. Rigneault *et al.*, All-dielectric silicon nanogap antennas to enhance the fluorescence of single molecules, *Nano Lett.* **16**, 5143 (2016).
- [23] D. Rocco, A. Lamprianidis, A. E. Miroshnichenko, and C. De Angelis, Giant electric and magnetic Purcell factor in dielectric oligomers, *J. Opt. Soc. Am. B* **37**, 2738 (2020).
- [24] Y. Yang, V. A. Zenin, and S. I. Bozhevolnyi, Anapole-assisted strong field enhancement in individual all-dielectric nanostructures, *ACS Photonics* **5**, 1960 (2018).
- [25] S. Mignuzzi, S. Vezzoli, S. A. Horsley, W. L. Barnes, S. A. Maier, and R. Sapienza, Nanoscale design of the local density of optical states, *Nano Lett.* **19**, 1613 (2019).
- [26] P. Albella, T. Shibanuma, and S. A. Maier, Switchable directional scattering of electromagnetic radiation with subwavelength asymmetric silicon dimers, *Sci. Rep.* **5**, 18322 (2015).
- [27] V. R. Almeida, Q. Xu, C. A. Barrios, and M. Lipson, Guiding and confining light in void nanostructure, *Opt. Lett.* **29**, 1209 (2004).
- [28] M. Galli, D. Gerace, A. Politi, M. Liscidini, M. Patrini, L. C. Andreani, A. Canino, M. Miritello, R. L. Savio, and A. Irrera *et al.*, Direct evidence of light confinement and emission enhancement in active silicon-on-insulator slot waveguides, *Appl. Phys. Lett.* **89**, 241114 (2006).
- [29] M. Galli, A. Politi, M. Belotti, D. Gerace, M. Liscidini, M. Patrini, L. Andreani, M. Miritello, A. Irrera, and F. Priolo *et al.*, Strong enhancement of  $\text{Er}^{3+}$  emission at

- room temperature in silicon-on-insulator photonic crystal waveguides, *Appl. Phys. Lett.* **88**, 251114 (2006).
- [30] Y. C. Jun, R. M. Briggs, H. A. Atwater, and M. L. Brongersma, Broadband enhancement of light emission in silicon slot waveguides, *Opt. Express* **17**, 7479 (2009).
- [31] P. Kolchin, N. Pholchai, M. H. Mikkelsen, J. Oh, S. Ota, M. S. Islam, X. Yin, and X. Zhang, High Purcell factor due to coupling of a single emitter to a dielectric slot waveguide, *Nano Lett.* **15**, 464 (2015).
- [32] N. Sakib and J. D. Ryckman, Design of ultra-small mode area all-dielectric waveguides exploiting the vectorial nature of light, *Opt. Lett.* **45**, 4730 (2020).
- [33] J. T. Robinson, C. Manolatou, L. Chen, and M. Lipson, Ultrasmall Mode Volumes in Dielectric Optical Microcavities, *Phys. Rev. Lett.* **95**, 143901 (2005).
- [34] H. Choi, M. Heuck, and D. Englund, Self-Similar Nanocavity Design with Ultrasmall Mode Volume for Single-Photon Nonlinearities, *Phys. Rev. Lett.* **118**, 223605 (2017).
- [35] S. Hu, M. Khater, R. Salas-Montiel, E. Kratschmer, S. Engelmann, W. M. Green, and S. M. Weiss, Experimental realization of deep-subwavelength confinement in dielectric optical resonators, *Sci. Adv.* **4**, eaat2355 (2018).
- [36] S. Lee, S. C. Eom, J. S. Chang, C. Huh, G. Y. Sung, and J. H. Shin, A silicon nitride microdisk resonator with a 40-nm-thin horizontal air slot, *Opt. Express* **18**, 11209 (2010).
- [37] R. Sun, P. Dong, N.-n. Feng, C.-y. Hong, J. Michel, M. Lipson, and L. Kimerling, Horizontal single and multiple slot waveguides: Optical transmission at  $\lambda = 1550$  nm, *Opt. Express* **15**, 17967 (2007).
- [38] H. T. Miyazaki and Y. Kurokawa, Squeezing Visible Light Waves into a 3-nm-Thick and 55-nm-Long Plasmon Cavity, *Phys. Rev. Lett.* **96**, 097401 (2006).
- [39] C. Ma, Q. Zhang, and E. Van Keuren, Analysis of symmetric and asymmetric nanoscale slab slot waveguides, *Opt. Commun.* **282**, 324 (2009).
- [40] This resonance condition is valid for waveguide modes with a near-zero reflection phase delay at the waveguide-air facets along the propagation direction. Otherwise, one should include both propagation phase delay and reflection phase delay.
- [41] C. Sauvan, J.-P. Hugonin, I. Maksymov, and P. Lalanne, Theory of the Spontaneous Optical Emission of Nanosize Photonic and Plasmon Resonators, *Phys. Rev. Lett.* **110**, 237401 (2013).
- [42] P. Lalanne, W. Yan, K. Vynck, C. Sauvan, and J.-P. Hugonin, Light interaction with photonic and plasmonic resonances, *Laser Photonics Rev.* **12**, 1700113 (2018).
- [43] P. T. Kristensen, C. Van Vlack, and S. Hughes, Generalized effective mode volume for leaky optical cavities, *Opt. Lett.* **37**, 1649 (2012).
- [44] K. Cognée, W. Yan, F. La China, D. Balestri, F. Intonti, M. Gurioli, A. Koenderink, and P. Lalanne, Mapping complex mode volumes with cavity perturbation theory, *Optica* **6**, 269 (2019).
- [45] P. Lalanne, W. Yan, A. Gras, C. Sauvan, J.-P. Hugonin, M. Besbes, G. Demésy, M. Truong, B. Gralak, and F. Zolla *et al.*, Quasinormal mode solvers for resonators with dispersive materials, *J. Opt. Soc. Am. A* **36**, 686 (2019).
- [46] W. L. Barnes, S. A. Horsley, and W. L. Vos, Classical antennas, quantum emitters, and densities of optical states, *J. Opt.* **22**, 073501 (2020).
- [47] See the Supplemental Material at <http://link.aps.org-supplemental/10.1103/PhysRevApplied.16.044065> for the SER enhancements of the emitter with variations of its lateral position, SER enhancement results of air-gap PGA with a glass support structure that include Refs. [36,59,60], SER enhancement results of PGAs on a glass substrate, and results for air-gap PGA in the receiving configuration.
- [48] E. V. Denning, J. Iiles-Smith, A. D. Osterkryger, N. Gregersen, and J. Mork, Cavity-waveguide interplay in optical resonators and its role in optimal single-photon sources, *Phys. Rev. B* **98**, 121306 (2018).
- [49] It should be noted that the emitter is at the position of peak field intensity for both resonant modes of the structure. Hence, the dipole mostly decays through coupling to the antenna modes and negligibly through direct coupling to free-space modes.
- [50] L. K. Warne, L. I. Basilio, W. L. Langston, W. A. Johnson, and M. B. Sinclair, Perturbation theory in the design of degenerate rectangular dielectric resonators, *Prog. Electromagn. Res.* **44**, 1 (2012).
- [51] I. Staude, A. E. Miroshnichenko, M. Decker, N. T. Fofang, S. Liu, E. Gonzales, J. Dominguez, T. S. Luk, D. N. Neshev, and I. Brener *et al.*, Tailoring directional scattering through magnetic and electric resonances in subwavelength silicon nanodisks, *ACS Nano* **7**, 7824 (2013).
- [52] W. Liu and Y. S. Kivshar, Generalized Kerker effects in nanophotonics and meta-optics, *Opt. Express* **26**, 13085 (2018).
- [53] C. A. Balanis, *Antenna Theory: Analysis and Design* (John Wiley & Sons, New York, 2016).
- [54] S. Wakui, J. Nakamura, and A. Natori, First-principles calculations of dielectric constants for ultrathin SiO<sub>2</sub> films, *J. Vac. Sci. Technol. B* **24**, 1992 (2006).
- [55] L. Keldysh, Coulomb interaction in thin semiconductor and semimetal films, *J. Exp. Theor. Phys. Lett.* **29**, 658 (1979).
- [56] P. Pursula, M. Hirvonen, K. Jaakkola, and T. Varpula, Antenna effective aperture measurement with backscattering modulation, *IEEE Trans. Antennas Propag.* **55**, 2836 (2007).
- [57] The spectral-directivity values of PGAs in the receiving configuration are similar to those of transmission. However, the two values differ from each other when the emitter is weakly coupled to the resonant modes of the structure. For an accurate characterization of directivity during reception, the resonant modes should be excited by a plane wave propagating toward the structure in the desired direction.
- [58] A. Patri, K. G. Cognée, D. M. Myers, L. Haeberlé, V. Menon, and S. Kéna-Cohen, Hybrid epsilon-near-zero modes of photonic gap antennas, arXiv preprint [ArXiv:2107.10301](https://arxiv.org/abs/2107.10301) (2021).
- [59] S. Liu, K. Srinivasan, and J. Liu, Nanoscale positioning approaches for integrating single epitaxial quantum emitters with photonic nanostructures, arXiv preprint [ArXiv:2105.05479](https://arxiv.org/abs/2105.05479) (2021).
- [60] C. Toninelli, I. Gerhardt, A. Clark, A. Reserbat-Plantey, S. Götzinger, Z. Ristanović, M. Colautti, P. Lombardi, K. Major, and I. Deperasińska *et al.*, Single organic molecules for photonic quantum technologies, *Nat. Mater.* **1** (2021).